Bloch oscillation phases investigated by multipath Stückelberg atom interferometry

Tahiyat Rahman [1], Anna Wirth-Singh,[1] Andrew Ivanov,[2] Daniel Gochnauer [1], Emmett Hough [1], and Subhadeep Gupta[1]

[1]*Department of Physics, University of Washington, Seattle, Washington 98195, USA*
[2]*Department of Physics, California Institute of Technology, Pasadena, California 91125, USA*

Atoms undergoing Bloch oscillations (BOs) in an accelerating optical lattice acquire momentum of two photon recoils per BO. This technique provides a large momentum transfer tool for atom optics, but its full exploitation for atom interferometric sensors requires both experimental and theoretical characterization of associated phases. Each BO involves a Landau-Zener crossing with multiple crossings inducing interference known as Stückelberg interference. We develop a multipath Stückelberg interferometer and investigate atomic phase evolution during BOs, up to 100 photon recoil momentum transfer. We compare to numerically calculated single-particle Schrödinger evolution, demonstrate highly coherent BO sequences, and assess phase stability requirements for BO-enhanced precision interferometry in fundamental physics and sensing applications.

Bloch oscillations (BOs) of cold atoms in an optical lattice [1,2] have emerged as a powerful tool in quantum metrology. Local gravity measurements [3] and equivalence principle tests [4] rely on sensing the external force through measurement of consequent BO frequency, while large momentum transfer (LMT) engineered by optically synthesizing efficient BOs plays a central role in tests of quantum electrodynamics [5,6]. In the latter case, LMT-BOs increase the momentum separation of two different atom interferometers (AIs). High-efficiency LMT-BOs *within* an AI generate what we will call "BO-enhanced" AI and have the potential to create very large interferometer space-time areas for next generation fundamental physics tests and applications in inertial sensing and gradiometry [7].

The central appeal for employing BOs for LMT applications compared to other techniques such as pulsed Bragg diffraction [8,9] lies in the high efficiency acceleration possible with BO dynamics restricted to a single lattice energy band, well separated in energy from other bands. However, this feature is also accompanied by large phase accumulation in this band during the LMT-BO process relative to another band. This can increase demands on experimental controls to maintain phase stability in a BO-enhanced AI composed of paths that lie in these two bands. While $1000\hbar k$ level momentum transfer has been demonstrated with BOs [5,10], ($\hbar k$ is the lattice photon momentum), BO-enhanced AI has been limited to relatively modest arm separation ($<100\hbar k$) [11–16]. Continued development of LMT-BO thus relies crucially on the experimental characterization of phases associated with BO processes. Earlier experimental measurements of such

differential phases on AI paths have been limited to $N_{BO} \leqslant 2$ where N_{BO} is the number of BOs [17].

Here we investigate the phase associated with LMT-BO processes by utilizing the fact that each BO is accompanied by a Landau-Zener (LZ) crossing which acts as a beamsplitter between the quantum mechanically coupled levels or bands. We use the interference signal from multiple LZ crossings, known as Landau-Zener-Stückelberg interference [18–21] or simply Stückelberg interference, to perform multipath Stückelberg interferometry (MPSI) on a Bose-Einstein condensate (BEC) atom source. The AI paths are composed of atomic wavefunction amplitudes evolving along Bloch bands during an LMT-BO sequence. We find that the MPSI exhibits a characteristic temporal interference pattern from relative Stückelberg phase accruals on different AI paths, in very good agreement with coherent, single-particle Schrödinger evolution for both ground and excited band BO. Distinct from earlier demonstrations with ultracold atoms that were limited to two-path Stückelberg interference [22,23], our observations persist even for $N_{BO} = 50$, well into the regime of relevance for precision AI.

Our experimental procedures build on previous work [24,25] with additional details provided in [26]. Briefly, we produce ^{174}Yb BECs with 7×10^4 atoms in an optical dipole trap (ODT). After the BEC is prepared, the ODT is switched off and the atoms are allowed to freely expand for a time t_{exp} before encountering a vertical optical lattice which is adiabatically turned on over a time $t_{ramp} = 300\,\mu s$. The value of t_{exp} is chosen to be sufficiently large for all the initial atomic interaction energy to be converted into kinetic energy [27], while keeping the cloud size ($<50\,\mu m$) much smaller than the lattice beams.

The lattice is formed from a pair of counter-propagating laser beams oriented 5 mrad with respect to gravity, with a waist of 1.8 mm. The lattice beams are detuned by $\Delta \simeq -3500\,\Gamma$ from the 556 nm intercombination transition, where $\Gamma = 2\pi \times 182\,kHz$, yielding a lattice spacing
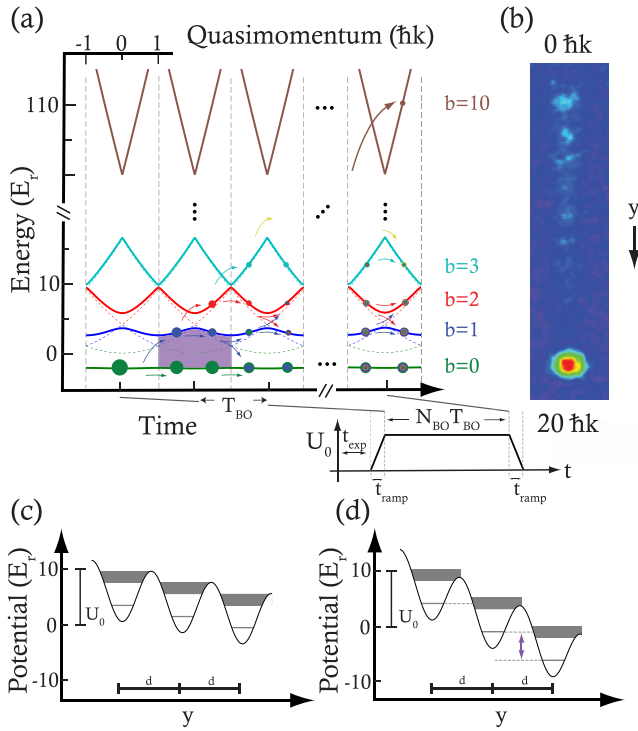
FIG. 1. Multipath Stückelberg interferometer scheme. (a) Atomic passage in an extended Brillouin zone picture with avoided band crossings acting as beamsplitters, shown for $U_0/E_r = 10$ and $N_{BO} = 10$. The shaded region highlights the energy difference between $b = 0$ and 1 within one Brillouin zone. Inset shows applied lattice intensity variation. (b) Absorption image ($t_{exp} = 3$ ms, 12 ms TOF, three-shot average) showing MPSI output of ten momentum states for $N_{BO} = 10$, $U_0/E_r = 6$, $T_{BO} = 0.33(h/E_r)$. Gravity points in the $-y$ direction. (c) Effective spatial potential showing three lattice sites for $U_0/E_r = 10$ and $T_{BO} = 0.5(h/E_r)$. The shading represents the bandwidth. (d) Same as (c) but for $T_{BO} = 0.2(h/E_r)$. In this case, the ground state in a site is degenerate with the first excited state in an adjacent site, corresponding to a 2π phase difference between $b = 0$ and 1 during one BO.

$d = \pi/k = 278$ nm, and a peak spontaneous scattering rate per E_r of lattice depth of $R_s = 2\pi \times 1.1$ Hz. Here $E_r = h^2/8md^2 = h \times 3.7$ kHz is the single photon recoil energy. Upon reaching the targeted depth U_0, the lattice intensity is kept constant during the interferometry sequence, and subsequently ramped down in 300 µs. To counter the effect of atomic free fall and provide a stationary lattice in the comoving frame, the relative frequency δ of the lattice laser beams is chirped at the rate $\dot{\delta}_g = 2\pi g/d$ during the entire duration of lattice application, including during the intensity ramps. Here g is the acceleration due to gravity. During the interferometry sequence, in addition to $\dot{\delta}_g$ we apply a variable frequency chirp $\dot{\delta}_{BO}$ which drives BOs, accelerating atoms relative to the free-fall frame in the $+y$ direction. The adiabatic lattice ramp-down maps the band populations to corresponding populations in free-particle momentum states, which are then observed in time-of-flight (TOF) absorption imaging.

Our MPSI (see Fig. 1) probes the action of a sequence of N_{BO} Bloch oscillations driven by the frequency chirp $\dot{\delta}_{BO}$ in a

lattice of depth U_0. In the lattice frame, the atoms experience a periodic potential and an effective constant force which drives BOs. The corresponding tilt of the periodic potential in the freely falling frame is uniquely determined by $\dot{\delta}_{BO}$ and the ensuing BOs have period $T_{BO} = 8E_r/(\hbar\dot{\delta}_{BO})$. The single particle dynamics in this frame are thus described by the Hamiltonian

$$\hat{H} = \frac{\hat{p}^2}{2m} + U_0\cos^2\left(\pi\frac{\hat{y}}{d}\right) - \frac{h}{T_{BO}}\frac{\hat{y}}{d}. \tag{1}$$

In Fig. 1(a) we present the MPSI in an extended Brillouin zone scheme. For most of our work, we load the atomic cloud into the ground band $b = 0$ of the lattice at quasimomentum $q = 0$, before initiating the linear frequency sweep $\dot{\delta}_{BO}$. The initial velocity width is less than 10% of the Brillouin zone. Each avoided crossing acts as a coherent beamsplitter where an interband transition may occur. Equivalently, the atoms experience the Hamiltonian of Eq. (1) during this sweep time set by $N_{BO} \times T_{BO}$. The representative TOF absorption image shown in Fig. 1(b) displays the different output ports of the MPSI as populations of free-particle states separated by multiples of two photon recoils ($\gg$ velocity width), mapped from the corresponding Bloch band states. Since ground band BOs have one avoided crossing per Brillouin zone, this interference geometry generates $2^{N_{BO}-1}$ paths considering only the lowest two bands. Since band numbers up to $b = N_{BO}$ may be populated leading to many additional paths [28,29], this power scaling is a lower bound on the total number of interfering paths. In Figs. 1(c) and 1(d), we show two representative examples of the tilted potential corresponding to two different values of $\dot{\delta}_{BO}$.

We first demonstrate MPSI for ground band BOs with $N_{BO} = 10$, a sequence large enough to capture the steady-state $N_{BO} \to \infty$ behavior. As shown in Fig. 2(a), the interferometer output, equivalently the 10-BO efficiency, exhibits oscillatory behavior as a function of T_{BO} for various lattice depths. The N_{BO} efficiency is defined as the fraction of the total atom number accelerated to momentum $2N_{BO}\hbar k$ by the frequency chirp $\dot{\delta}_{BO}$. A standard analysis associates each avoided crossing with an LZ tunneling process [18,30] depleting *population* incoherently from $b = 0$ leading to the prediction of $[1 - \exp\{-\pi^2 E_{bg}^2 T_{BO}/(8hE_r)\}]^{N_{BO}}$ for the overall BO efficiency. Here E_{bg} is the depth-dependent band gap [31]. As shown by the dashed lines in Fig. 2(a), the LZ prediction agrees with the observed overall trend with T_{BO} and U_0, but fails to capture any of the nonmonotonic behavior.

This nonmonotonic behavior is the signature of multipath Stückelberg oscillations. The alternating local extrema at depth-dependent T_{BO} locations correspond to constructive and destructive interference of the contributing paths. To quantitatively understand our observations, we perform numerical simulations of a single particle evolving in the Hamiltonian of Eq. (1) [26]. We additionally incorporate a small contribution from spontaneous scattering with the multiplicative factor $\exp[-R_s(U_0/2E_r)(\alpha t_{ramp} + N_{BO}T_{BO})]$. Here $\alpha = 0.74$ is a numerical factor accounting for the specific shape of intensity ramps used [26]. The good agreement of these simulations [thin solid lines in Fig. 2(a)] with our observations indicates a high degree of coherence in our MPSI.
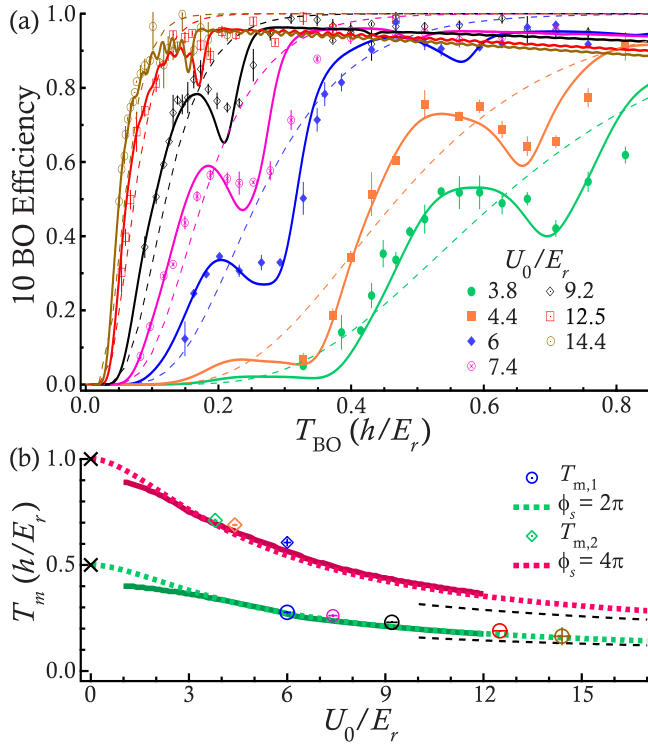
FIG. 2. MPSI signal for various lattice depths. (a) Observed ten BO efficiency variation with $T_{BO} = 8E_r/(\hbar\delta_{BO})$. Solid lines show the corresponding numerical simulations of Eq. (1), including spontaneous scattering. Dashed lines show predictions of the Landau-Zener model. (b) Locations of first ($T_{m,1}$) and second ($T_{m,2}$) Stückelberg oscillation minima as a function of depth. Markers and solid lines are extracted respectively from experimental data shown in (a) and numerical simulations. Colored dotted lines correspond to setting $\phi_S = 2\pi$ and 4π in Eq. (2) for $b = 0$. The T_m predictions for a free particle ($U_0 \rightarrow 0$) are shown by the black crosses and for the harmonic approximation ($U_0 \rightarrow \infty$) by the black dashed lines.

The interference patterns in Fig. 2(a) represent MPSI measurements of Stückelberg phase accrual during BO sequences. For ground band BO, ϕ_S is the relative phase between a path which traverses $b = 1$ and another which traverses $b = 0$ [from the energy difference indicated by the shaded region in Fig. 1(a)]:

$$\phi_S^{(b)}(U_0) = \frac{E_r T_{BO}}{\hbar}\mathcal{I}^{(b)}, \tag{2}$$

where $\mathcal{I}^{(b)} = \frac{1}{2E_r}\int_{-1}^{1}[E^{(b+1)}(q, U_0) - E^{(b)}(q, U_0)]dq$ and $E^{(b)}(q, U_0)$ is the q-dependent energy in band b for lattice depth U_0. The location of the pronounced interference minima or depletion in $b = 0$ can be estimated by setting the Stückelberg phase ϕ_S during one BO to an even multiple of π, corresponding to constructive interference into $b = 1$. The first and second minima locations determined by the T_{BO} values that solve $\phi_S = 2\pi$ and 4π respectively in Eq. (2) are shown as the solid lines in Fig. 2(b), in clear agreement with the experimentally observed minima locations $T_{m,1}$ and $T_{m,2}$. The dotted lines result from the numerical simulation of Eq. (1) and show excellent agreement with the Stückelberg phase calculations using Eq. (2), except at the lowest depths.
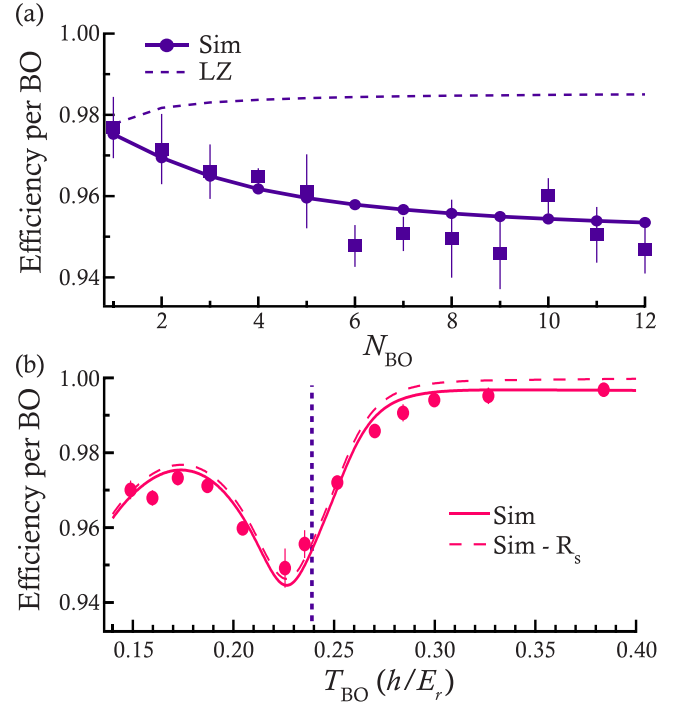

FIG. 3. Evolution of Stückelberg interference visibility with N_{BO}. (a) Per-BO efficiency vs N_{BO} at fixed $T_{BO} = 0.24(h/E_r)$ near $T_{m,1}$ for $U_0/E_r = 8$. Experimental data are shown as square markers and corresponding numerical simulations including spontaneous scattering as points connected by lines. The dashed line is the Landau-Zener prediction including spontaneous scattering. (b) MPSI signal displayed as per-BO efficiency for an $N_{BO} = 50$ LMT-BO sequence with $U_0/E_r = 8.3$. The solid (dashed) curve represents the corresponding numerical simulation with (without) spontaneous scattering. The vertical dashed line marks the T_{BO} value in (a).

The deviations for $U_0 \lesssim 3E_r$ arise from the contribution of the Stokes phase [23,32–34].

The fact that Eq. (2) accurately predicts the signal minima emphasizes a resonant effect also found in other multipath matter-wave interference phenomena such as the temporal Talbot effect [35] and the quantum kicked rotor [36]. Somewhat surprisingly, these resonances remain pronounced even for large depths $U_0 > 10E_r$ when the avoided crossing locations in momentum space, and therefore the beamsplitter timings, are less sharply defined due to band flatness. In this regime, intuition can be gained from the position space picture [Figs. 1(c) and 1(d)] and spatial tunneling into neighboring sites of the lattice. The position space visualization for $T_{m,1}$ is shown in Fig. 1(d) and corresponds to resonant tunneling loss into nearest neighbor sites. Likewise, $T_{m,2}$ corresponds to resonant tunneling to next-nearest neighbor at half the lattice tilt as $T_{m,1}$.

We now turn to the dependence of the MPSI signal on N_{BO}. As schematically shown in Fig. 1(a) and discussed above, the MPSI involves $>2^{N_{BO}-1}$ interfering paths. Even assuming perfectly coherent evolution, this leads to a saturation of the MPSI signal as $N_{BO} \rightarrow \infty$. In Fig. 3(a), we show the evolution of efficiency per BO for a fixed T_{BO} as N_{BO} is varied. The per-BO efficiency is defined as the $(1/N_{BO})^{th}$ power of the measured N_{BO} efficiency. In order to increase the dynamic

range for this study, the T_{BO} is chosen near a strong interference feature, leading to an observation of the growth of Stückelberg visibility. The signal starts to saturate around $N_{BO} = 10$, reflecting the fact that even though the number of paths contributing to it at least doubles per subsequent BO, the signal in $b = 0$ is composed primarily of paths that were generated within the last ten BOs. The numerical simulation (points joined by lines) is in good agreement with observations. The deviation from the LZ result (dashed line) grows with increasing N_{BO}.

In Fig. 3(b) we show a representative MPSI signal for $N_{BO} = 50$ at a similar depth. Clearly, the visibility remains strong and the agreement with the theoretical model is excellent, with a very small contribution from spontaneous scattering. The vertical dashed line marks the T_{BO} location of Fig. 3(a).

Having established the high coherence of long BO sequences using MPSI, we now examine implementation criteria relevant for high precision BO-enhanced AI. For this, one needs to consider both the band number separation ($= N_{BO}$) *and* the relative phase evolution Φ of two paths from an LMT-BO sequence applied on one of the paths. Fast and high efficiency Bloch oscillation will be achieved at high lattice depths. The $U_0/E_r = 14.4$ data shown in Fig. 2(a) indicates 0.995 efficiency per $\hbar k$ momentum transfer delivered at 23 μs per $\hbar k$ [$T_{BO} \simeq 0.17(h/E_r)$]. This is considerably higher than the 0.984 efficiency per $\hbar k$ achieved with optimized Bragg diffraction pulses at the same delivery rate of LMT in precision AI with the same atomic species in [24]. At $U_0/E_r = 25.5$ we measure even higher LMT-BO efficiency of 0.999 per $\hbar k$ delivered at twice the rate [26]. This corresponds to a $1000\hbar k$ LMT efficiency of 0.47 delivered in 11 ms. The corresponding efficiency achieved in [24] using Bragg diffraction scales to the impractical 10^{-7}, although higher performance may be achievable in the future through numerical quantum optimal control [37].

Taking $1000\hbar k$ as a benchmark for next generation high-precision BO-enhanced AIs, we now consider the implications on AI phase from technical considerations of lattice intensity noise. At high depth $U_0 \gg E_r$ and for $N_{BO} \gg 1$, we have $\Phi \simeq \frac{U_0}{2\hbar}T_{BO}N_{BO}$ [26], and the corresponding phase noise is $\delta\Phi \simeq \epsilon\Phi$ where ϵ is the relative intensity noise in the lattice beams. We take 100 mrad standard deviation as the benchmark for AI phase stability, which is about an order of magnitude below the standard deviation from random phase measurements between zero and π. For the $1000\hbar k$ example discussed above, achieving $\delta\Phi$ of 100 mrad will require $\epsilon = 3 \times 10^{-5}$, which is experimentally challenging. Excited band BOs at "magic" depths optimized to suppress phase noise induced by lattice intensity variation [17] can help address this challenge.

We finally discuss our experiments on measuring BO phases in excited bands. For this we modify the MPSI sequence by loading the atomic cloud away from avoided crossings at $q = 1/2$ in $b = 1$ [Fig. 1(a)] [17]. The results for two different depths are shown in Fig. 4. The observed Stückelberg patterns are similar to those seen in the ground band and are again in good agreement with the numerical simulations. Since the avoided crossings between $b = 1$ and 2 feature smaller energy gaps than those between $b = 1$ and 0,
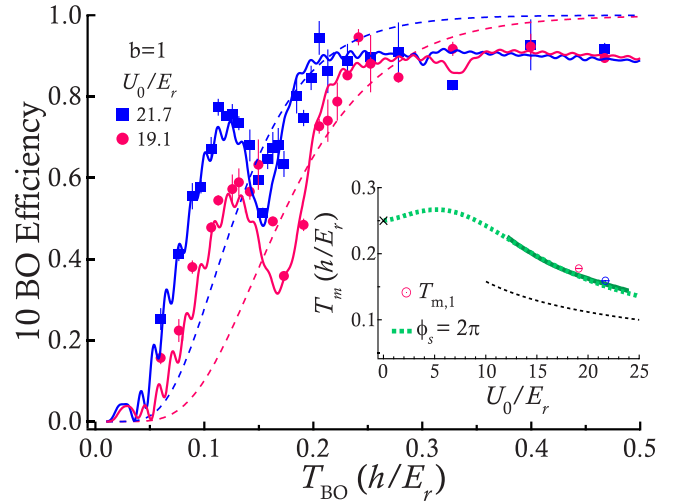

FIG. 4. MPSI signal for excited band. Main figure shows observed ten BO efficiency variation with $T_{BO} = 8E_r/(\hbar\delta_{BO})$ for $b = 1$ and two different U_0. Solid lines show corresponding numerical simulations of Eq. (1), including spontaneous scattering. Dashed lines show predictions of the Landau-Zener model. Inset shows location of Stückelberg oscillation minima $T_{m,1}$ as a function of depth. Markers and solid lines are extracted respectively from experimental data shown in the main figure and numerical simulations. The colored dotted line corresponds to setting $\phi_S = 2\pi$ in Eq. (2) for $b = 1$. The $T_{m,1}$ prediction for a free particle ($U_0 \to 0$) is shown by the black cross and for the harmonic approximation ($U_0 \to \infty$) by the black dashed line.

more amplitude from $b = 1$ goes to $b = 2$ than to $b = 0$. We would thus expect that the MPSI signal is dominated by the amplitudes in $b = 1$ and 2 rather than $b = 1$ and 0, and this is verified by comparing the locations of the interference minima $T_{m,1}$ to the condition $\phi_S = 2\pi$ with $b = 1$ in Eq. (2) (see Fig. 4 inset). An additional high-frequency oscillation is also seen in the numerical simulation, with a weak amplitude which is below our experimental detection limit. It can be related to the phase accumulation between paths that remain in $b = 1$ and $b = 2$ throughout the MPSI.

In summary, we developed a multipath Stückelberg interferometer with ultracold atoms and used it to study the phase imparted during a long sequence of BOs, thus enhancing the toolbox and providing guidance for next-generation fundamental physics tests, gravimetry, and inertial sensing with AI. We demonstrated that BO processes can be applied in a highly coherent manner, implying that the use of large N_{BO} as LMT beamsplitters is limited only by technical effects. The MPSI tool can help optimize atom-optics parameters in BO-enhanced AIs and also be used to explore geometric phases in topologically nontrivial band structures [38]. Furthermore, we identify phase noise stemming from lattice intensity fluctuations as an important technical challenge for the future, which could be addressed by excited band BOs at magic depths [17], symmetric AI geometries [14,15], or alternative LMT approaches such as Floquet atom optics [39].

While completing work on this manuscript, we became aware of related theoretical work in [40], where spatial Wannier-Stark wavefunctions are used to address the high

[1] M. Ben Dahan, E. Peik, J. Reichel, Y. Castin, and C. Salomon, Bloch oscillations of atoms in an optical potential, Phys. Rev. Lett. **76**, 4508 (1996).

[2] S. R. Wilkinson, C. F. Bharucha, K. W. Madison, Q. Niu, and M. G. Raizen, Observation of atomic Wannier-Stark ladders in an accelerating optical potential, Phys. Rev. Lett. **76**, 4512 (1996).

[3] N. Poli, F.-Y. Wang, M. G. Tarallo, A. Alberti, M. Prevedelli, and G. M. Tino, Precision measurement of gravity with cold atoms in an optical lattice and comparison with a classical gravimeter, Phys. Rev. Lett. **106**, 038501 (2011).

[4] M. M. Tarallo, T. Mazzoni, N. Poli, X. Zhang, D. V. Sutyrin, and G. M. Tino, Test of Einstein equivalence principle for 0-spin and half-integer-spin atoms: Search for spin-gravity coupling effects, Phys. Rev. Lett. **113**, 023005 (2014).

[5] L. Morel, Y. Zhao, P. Cladé, and S. Guellati-Khélifa, Determination of the fine-structure constant with an accuracy of 81 parts per trillion, Nature (London) **588**, 61 (2020).

[6] R. H. Parker, C. Yu, B. Estey, W. Zhong, and H. Müller, Measurement of the fine-structure constant as a test of the Standard Model, Science **360**, 191 (2018).

[7] G. Tino and M. Kasevich, Atom interferometry, *Proceedings of the International School of Physics "Enrico Fermi"* (IOS Press, Washington, DC, 2014).

[8] M. Kozuma, L. Deng, E. W. Hagley, J. Wen, R. Lutwak, K. Helmerson, S. L. Rolston, and W. D. Phillips, Coherent splitting of Bose-Einstein condensed atoms with optically induced Bragg diffraction, Phys. Rev. Lett. **82**, 871 (1999).

[9] S. Gupta, A. E. Leanhardt, A. D. Cronin, and D. E. Pritchard, Coherent manipulation of atoms with standing light waves, C. R. Acad. Sci. IV-Phys. **2**, 479 (2001).

[10] M. Cadoret, E. de Mirandes, P. Cladé, and S. Guellati-Khélifa, C. Schwob, F. Nez, L. Julien, and F. Biraben, Combination of Bloch oscillation with a Ramsey-Bordé interferometer: New determination of the fine-structure constant, Phys. Rev. Lett. **101**, 230801 (2008).

[11] P. Cladé, S. Guellati-Khélifa, F. Nez, and F. Biraben, Large momentum beam splitter using Bloch oscillations, Phys. Rev. Lett. **102**, 240402 (2009).

[12] H. Müller, S.-W. Chiow, S. Herrmann, and S. Chu, Atom interferometers with scalable enclosed area, Phys. Rev. Lett. **102**, 240403 (2009).

[13] G. D. McDonald, C. C. N. Kuhn, S. Bennetts, J. E. Debs, K. Hardman, M. Johnsson, J. D. Close, and N. P. Robins, 80ℏk momentum separation with Bloch oscillations in an optically guided atom interferometer, Phys. Rev. A **88**, 053620 (2013).

[14] Z. Pagel, W. Zhing, R. H. Parker, C. T. Olund, N. Y. Yao, C. Yu, and H. Müller, Symmetric Bloch oscillations of matter waves, Phys. Rev. A **102**, 053312 (2020).

[15] M. Gebbe, J.-N. Siemß, M. Gersemann, H. Müntinga, S. Herrmann, C. Lämmerzahl, H. Ahlers, N. Gaaloul, C.

Schubert, K. Hammerer, S. Abend, and E. M. Rasel, Twin-lattice atom interferometry, Nat. Commun. **12**, 2544 (2021).

[16] Ground-band BOs have been used to demonstrate a phase-stable 80ℏk AI in a guided (nonfree space) geometry [13]. Recent work in free-space AIs has shown even larger momentum splitting with ground-band BOs [14,15], however, phase stability was demonstrated only up to 20ℏk.

[17] K. E. McAlpine, D. Gochnauer, and S. Gupta, Excited-band Bloch oscillations for precision atom interferometry, Phys. Rev. A **101**, 023614 (2020).

[18] C. Zener, Non-adiabatic crossing of energy levels, Proc. R. Soc. London A **137**, 696 (1932).

[19] E. C. G. Stuckelberg, Theory of inelastic collisions between atoms, Helv. Phys. Acta **5**, 369 (1932).

[20] W. D. Oliver, Y. Yu, J. C. Lee, K. K. Berggren, L. S. Levitov, and T. P. Orlando, Mach-Zehnder interferometry in a strongly driven superconducting qubit, Science **310**, 1653 (2005).

[21] T. Ota, K. Hitachi, and K. Muraki, Landau-Zener-Stückelberg interference in coherent charge oscillations of a one-electron double quantum dot, Sci. Rep. **8**, 5491 (2008).

[22] S. Kling, T. Salger, C. Grossert, and M. Weitz, Atomic Bloch-Zener oscillations and Stückelberg interferometry in optical lattices, Phys. Rev. Lett. **105**, 215301 (2010).

[23] A. Zenesini, D. Ciampini, O. Morsch, and E. Arimondo, Observation of Stückelberg oscillations in accelerated optical lattices, Phys. Rev. A **82**, 065601 (2010).

[24] B. Plotkin-Swing, D. Gochnauer, K. E. McAlpine, E. S. Cooper, A. O. Jamison, and S. Gupta, Three-path atom interferometry with large momentum separation, Phys. Rev. Lett. **121**, 133201 (2018).

[25] D. Gochnauer, T. Rahman, A. Wirth-Singh, and S. Gupta, Interferometry in an atomic fountain with ytterbium Bose-Einstein condensates, Atoms **9**, 58 (2021).

[26] See Supplemental Material at http://link.aps.org/supplemental/10.1103/PhysRevResearch.6.L022012 for further experimental and theoretical details.

[27] Y. Castin and R. Dum, Bose-Einstein condensates in time dependent traps, Phys. Rev. Lett. **77**, 5315 (1996).

[28] K. J. Hughes, J. H. T. Burke, and C. A. Sackett, Suspension of atoms using optical pulses, and application to gravimetry, Phys. Rev. Lett. **102**, 150403 (2009).

[29] M. Robert-de-Saint-Vincent, J.-P. Brantut, C. J. Bordé, A. Aspect, T. Bourdel, and P. Bouyer, A quantum trampoline for ultra-cold atoms, Europhys. Lett. **89**, 10002 (2010).

[30] J. H. Denschlag, J. E. Simsarian, H. Häffner, C. McKenzie, A. Browaeys, D. Cho, K. Helmerson, S. L. Rolston, and W. D. Phillips, A Bose-Einstein condensate in an optical lattice, J. Phys. B: At. Mol. Opt. Phys. **35**, 3095 (2002).

[31] D. Gochnauer, K. E. McAlpine, B. Plotkin-Swing, A. O. Jamison, and S. Gupta, Bloch-band picture for light-pulse atom diffraction and interferometry, Phys. Rev. A **100**, 043611 (2019).

[32] S. N. Shevchenko, S. Ashhab, and F. Nori, Landau-Zener-Stückelberg interferometry, Phys. Rep. **492**, 1 (2010).

[33] N. V. Vitanov, Transition times in the Landau-Zener model, Phys. Rev. A **59**, 988 (1999).

[34] O. V. Ivakhnenko, S. N. Shevchenko, and F. Nori, Nonadiabatic Landau-Zener-Stückelberg-Majorana transitions, dynamics, and interference, Phys. Rep. **995**, 1 (2023).

[35] L. Deng, E. W. Hagley, J. Deschlag, J. E. Simsarian, M. Edwards, C. W. Clark, K. Helmerson, S. L. Rolston, and W. D. Phillips, Temporal, matter-wave-dispersion Talbot effect, Phys. Rev. Lett. **83**, 5407 (1999).

[36] F. L. Moore, J. C. Robinson, C. F. Bharucha, B. Sundaram, and M. G. Raizen, Atom optics realization of the quantum δ-kicked rotor, Phys. Rev. Lett. **75**, 4598 (1995).

[37] G. Louie, Z. Chen, T. Deshpande, and T. Kovachy, Robust atom optics for Bragg atom interferometry, New J. Phys. **25**, 083017 (2023).

[38] L. K. Lim, J. N. Fuchs, and G. Montambaux, Mass and chirality inversion of a Dirac cone pair in Stückelberg interferometry, Phys. Rev. Lett. **112**, 155302 (2014).

[39] T. Wilkason, M. Nantel, J. Rudolph, Y. Jiang, B. E. Garber, H. Swan, S. P. Carman, M. Abe, and J. M. Hogan, Atom interferometry with Floquet atom optics, Phys. Rev. Lett. **129**, 183202 (2022).

[40] F. Fitzek, J.-N. Kirsten-Siemß, E. M. Rasel, N. Gaaloul, and K. Hammerer, Accurate and efficient Bloch-oscillation-enhanced atom interferometry, arXiv:2306.09399.